Article ID：1007−7294(2025)06−0863−15

Bottom Pressure Field Induced by Submerged Vehicle in Regular Waves

YI Wen−bin, *ZHANG Zhi−hong*, *DENG Hui*, *MENG Qing−chang*, *XIA Wei−xue*, *WANG Chong*, *LI Pei−hao*
(Basic Department, Naval University of Engineering, Wuhan 430033, China)

Abstract: The finite volume method was applied to numerically simulate the bottom pressure field induced by regular waves, vehicles in calm water and vehicles in regular waves. The solution of Navier-Stokes (N-S) equations in the vicinity of numerical wave tank's boundary was forced towards the wave theoretical solution by incorporating momentum source terms, thereby reducing adverse effects such as wave reflection. Simulations utilizing laminar flow, turbulent flow, and ideal fluid models were all found capable of effectively capturing the waveform and bottom pressure of regular waves, agreeing well with experimental data. In predicting the bottom pressure field of the submerged vehicle, turbulent simulations considering fluid viscosity and boundary layer development provided more accurate predictions for the stern region than inviscid simulations. Due to sphere's diffractive effect, the sphere's bottom pressure field in waves is not a linear superposition of the wave's and the sphere's bottom pressure field. However, a slender submerged vehicle exhibits a weaker diffractive effect on waves, thus the submerged vehicle's bottom pressure field in waves can be approximated as a linear superposition of the wave's and the submerged vehicle's bottom pressure field, which simplifies computation and analysis.

Key words: regular wave; submerged vehicle; bottom pressure field; numerical simulation
CLC number：U661.1 **Document code**：A **doi:** 10.3969/j.issn.1007−7294.2025.06.002

0 Introduction

The expansion of marine resource utilization necessitates enhanced monitoring of the underwater environment. With the escalation of submarine acoustic stealth capabilities, it is imperative to explore detection methods for non-acoustic physical fields, including light, electricity, magnetic fields, infrared radiation, thermal wakes, seismic waves, hydrodynamic pressure and gravity fields, to bolster the detection of underwater targets. The "hydrodynamic pressure field of a submerged vehicle" signifies the alteration in hydrodynamic pressure resulting from its movement, distinct from the conventional acoustic pressure field. Compared to acoustics and magnetic signals, the hydrodynamic pressure field's signal exhibits unique traits that resist elimination and is challenging to artificial emulation. Submerged vehicles exert a pronounced influence on the bottom pressure field compared to surface vessels. Employing pressure sensors along the seafloor to surveil the activities of submerged vehicles presents unique benefits. For example, the Swiss STL

Received date：2024−12−16
Foundation item：Supported by the Research Project of Naval University of Engineering (2022501220) and Hubei Provincial Natural Science Foundation (2024AFB954)
Biography：YI Wen-bin(1990–), male, associate professor, E-mail: yiwenbinhjgc@163.com; DENG Hui(1984–), female, professor, E-mail: denghui8411@163.com.

surveillance system has the capacity to detect underwater pressure signals[1]. Therefore, probing into the characteristics of the hydrodynamic pressure field of submerged vehicles, particularly the distribution of bottom pressure, is crucial for augmenting underwater detection capabilities.

Research on the characteristics of ship hydrodynamic pressure fields has been widely integrated into the design of mine warfare weapons. Bottom mines predominantly utilize pressure, acoustic, magnetic, and combined sensors as fuses, including the American MK55-6, the Italian MRP, the Japanese K1-K4 series, and the Taiwanese Wanxiang, among others. Jin[2] utilized the Hess-Smith approach to forecast changes in bottom pressure due to submerged vehicles, with the predicted results correlating well with experimental data. Deng[3–4] conducted an investigation into the dispersion, non-linearity, and time-variant effects of ship hydrodynamic pressure fields at different speeds in shallow water channels. High sea states can substantially impact the hydrodynamic pressure field[5]. However, prior studies have not contemplated the effects of incoming waves on ship hydrodynamic pressure fields. Lyu[6] analyzed the attenuation of regular wave hydrodynamic pressure fields with water depth using OpenFOAM software, identifying the influence range of wave-induced hydrodynamic pressure fields. Jiang[7] superimposed the hydrodynamic pressure field signals of target ship and waves to approximate the bottom pressure of ship in wave conditions, thereby investigating ship hydrodynamic pressure field detection technology. Despite the potential flow theory's basic solution adhering to the Laplace equation after superimposition, it may not conform to boundary conditions. Therefore, further research is required into the variation and coupling mechanisms of submerged vehicle hydrodynamic pressure fields in wave conditions.

In this study, the hydrodynamic pressure fields induced by regular waves and submerged vehicles both in calm water and in regular waves are predicted using numerical methods. The coupling mechanism between the hydrodynamic pressure field of the wave and that of the submerged vehicle is also analyzed. The findings could furnish a theoretical foundation and technical assistance for the advancement of underwater detection systems and mine pressure fuses.

1 Numerical methods

1.1 Governing equations

In the computation of turbulent flows, the RANS (Reynolds-Averaged Navier-Stokes) equations are employed for numerical solution, and the finite volume method is used to discretize the governing equations. Based on the Boussinesq hypothesis, the RANS equations for incompressible viscous fluid are as follows:

$$\frac{\partial u_i}{\partial x_i} = 0 \tag{1}$$

$$\frac{\partial}{\partial t}(\rho u_i) + \frac{\partial}{\partial x_j}(\rho u_j u_i) = -\frac{\partial p}{\partial x_i} + \frac{\partial}{\partial x_j}\left[(\mu + \mu_t)(\frac{\partial u_i}{\partial u_j} + \frac{\partial u_j}{\partial u_i})\right] + f_i \tag{2}$$

Eq. (1) and Eq. (2) are the continuity equation and momentum equation of incompressible viscous fluid, respectively, where u_i denotes the velocity component of fluid particles in the i direction, f_i represents the body force per unit mass, p is the pressure, μ is the fluid dynamic viscosity averaged over the phase volume fraction, and μ_t denotes the turbulent dynamic viscosity. These equations must be complemented with a turbulence model to render them solvable. For this study, the SST k-ω two-equation turbulence model[8], a widely-employed approach for turbulence computations, is selected. Additionally, the VOF (Volume of Fluid) multi-phase flow model[9], based on the theory of homogeneous equilibrium multi-phase flow, is utilized to track the interface between gas and liquid phases, with the HRIC (High Resolution Interface

Capturing) convective discretization scheme employed. The numerical simulations are carried out using STAR-CCM+ 2302 software.

In inviscid computations, both the dynamic viscosity of the fluid and the turbulent dynamic viscosity are set to zero. As a result, the momentum equations reduce to the Euler equations. These Euler equations are then numerically solved employing the finite volume method.

$$\frac{\partial}{\partial t}(\rho u_i)+\frac{\partial}{\partial x_j}(\rho u_j u_i)=-\frac{\partial p}{\partial x_i}+f_i \tag{3}$$

1.2 Wave model

Wave simulation is conducted using the fifth-order approximation of the Stokes wave theory, which provides a more accurate representation of real waves than the first-order Stokes wave theory. In this study, all simulated waves meet the criteria of the fifth-order Stokes wave theory, with an Ursell number less than 30. The Ursell number is defined as follows:

$$U_R=\frac{H\lambda^2}{d^3} \tag{4}$$

The wave surface of the Stokes fifth-order wave satisfies the following equation:

$$\zeta=\frac{1}{k}\sum_{n=1}^{5}\lambda_n\cos[n(kx-\omega t)] \tag{5}$$

The coefficients are as follows:

$$\begin{aligned}\lambda_1&=\lambda\\ \lambda_2&=\lambda^2B_{22}+\lambda^4B_{24}\\ \lambda_3&=\lambda^3B_{33}+\lambda^5B_{35}\\ \lambda_4&=\lambda^4B_{44}\\ \lambda_5&=\lambda^5B_{55}\end{aligned}$$

where H, λ, ω, d, and k denote the wave height, wavelength, circular frequency, water depth and wave number, respectively (Fig. 1), with remaining coefficients defined in Ref.[10].

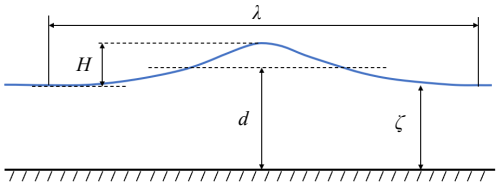

Fig.1 Wave profile of the Stokes fifth-order wave

Wave reflection at the end of the tank can cause significant interference throughout the entire domain, disrupting the wave patterns. To mitigate this issue, two methods are typically utilized in numerical simulations: one involves applying damping to the vertical motion of the fluid at the end of the numerical wave tank, thereby expediting wave decay, and is known as wave damping[11]; the other involves introducing momentum source terms near the boundary of the numerical wave tank to align the solution of the discretized Navier-Stokes (N-S) equations with the theoretical or simplified numerical wave solution. The latter method, known as wave forcing[12], is used in this study. In the area near the object, the N-S equations are still solved. The wave forcing method introduces momentum source terms into the N-S equations in the following form:

$$q_\phi=-\gamma\rho(\phi-\phi^*) \tag{6}$$

where ρ is the fluid density, ϕ represents the current solution to the N-S equations, ϕ^* signifies the theoretical solution for waves. The wave forcing coefficient γ decreases gradually from the boundary to the core area, which satisfies the following rules :

$$\gamma=-\gamma_0\cos\left(\frac{\pi x^*}{2}\right) \tag{7}$$

where x^* signifies the distance from the boundary, normalized by the wave forcing length.

Wave forcing zone is shown in Fig. 2. Wave forcing method achieved by introducing momentum source terms can result in a distortion of the pressure distribution at the bottom. Therefore, the region where wave forcing is applied should be positioned away from the submerged vehicle.

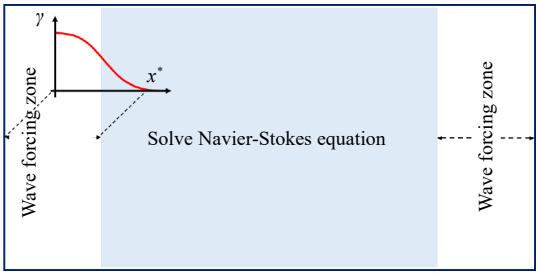

Fig.2 Wave forcing zone

2 Numerical methods validation

2.1 Regular waves hydrodynamic pressure field

The water tank's depth d is 2 m. The regular wave's wavelength λ is 8.0 m, the wave height H is 0.025 m, and the wave period T is 2.36 s. The computations are based on the fifth-order approximation of Stokes' wave theory. The computational domain spans five times the wave's wavelength in length and 0.05 m in width. The inflow and outflow boundaries are both set as velocity inlets, the top boundary as a pressure outlet, the bottom as a free-slip wall, and the side boundaries as symmetry. To ensure wave stability and prevent reflections at the boundaries, a wave forcing region is established 1 wavelength away from the inflow and outflow boundaries[13]. Fig. 3 shows the side view of the computational domain.

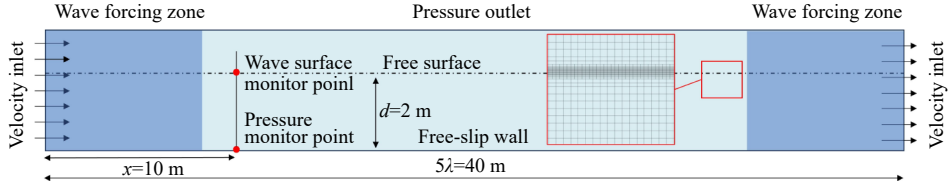

Fig.3 Computational domain of wave tank (Side view)

Tab.1 shows wave properties and numerical discretization. The spatial discretization is conducted using a trimmed cell mesher, resulting in a total of 2 million grid nodes. To accurately capture the wave pattern's variations, the grid near the waterline is refined. In the vertical (z-) direction, the grid spacing is set at 1/16 of

Tab.1 Wave properties and numerical discretization

Wave properties	Wave type	Stokes fifth-order wave
	Wave length λ	8.0 m
	Wave height H	0.025 m
	Wave period T	2.36 s
	Water depth d	2 m
Computational domain	Length×height×width	40 m×3 m×0.05 m
Spatial discretization	Grid type	Trimmed cell mesh
	Grid nodes	2 million
	Grid aspect ratio	≤8
	Grid refinement	16 cells per wave height 625 cells per wave length
Time discretization	Discretization scheme	Second-order implicit scheme
	Time step	0.002 s
	Maximum internal iterations per time step	10
	Maximum Courant number	0.4

the wave height, while in the horizontal (x-) direction, it is 1/625 of the wave length, yielding a grid aspect ratio of 8∶1. Time discretization employs a second-order implicit scheme with a time step of 0.002 s. The maximum number of internal iterations per time step is limited to 10, and the maximum Courant number throughout the computation is maintained below 0.4.

Fig. 4 presents a comparison of wave pattern results from the laminar model, SST turbulence model, and inviscid fluid model. Fig. 5 illustrates the bottom pressure distribution under these three computation settings, with pressure units expressed in mmH_2O. The monitor point is 10 m away from inlet boundary, as shown in Fig. 3. It is noted that the wave patterns and bottom pressure predictions from these configurations are almost identical, suggesting that viscosity has a minimal impact on wave simulation. Fig. 6 shows wave pattern prediction with SST model. The wave height remains quite stable after 12 s propagation. Fig. 7 contrasts the wave patterns and bottom pressure computed using the SST turbulence model with experimental data[13], illustrating a notable degree of agreement between the computational and experimental values. The simulated values of wave pattern and bottom pressure are steady over time, while the measured values vary slightly over time. The maximum deviation is within 10%, suggesting that the current computational setup can reliably predict wave hydrodynamic pressure fields.

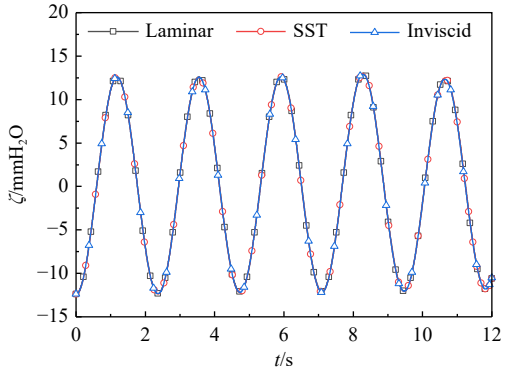

Fig.4 Wave pattern comparison under different computation settings

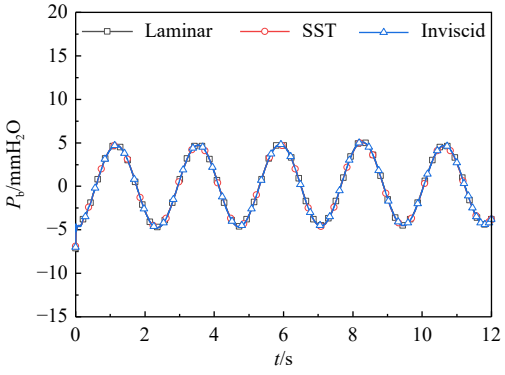

Fig.5 Comparison of bottom pressure under different computation settings

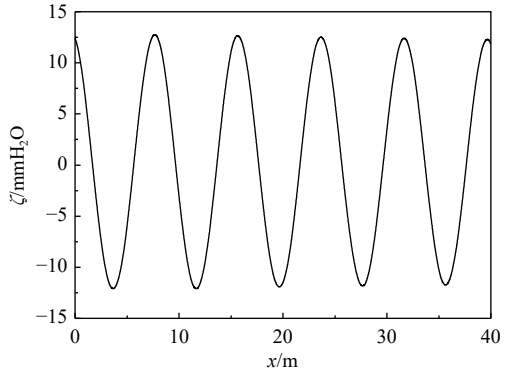

Fig.6 Wave pattern prediction with SST model

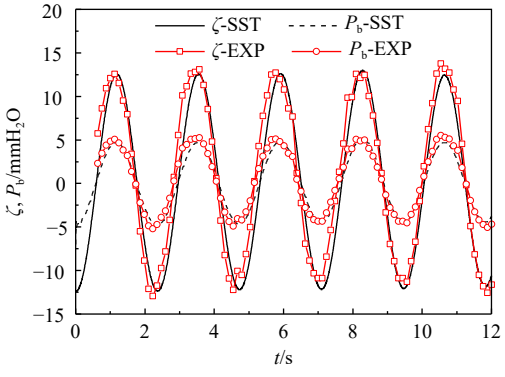

Fig.7 Simulated and measured values of wave pattern and bottom pressure

2.2 Submerged vehicle hydrodynamic pressure field

The submerged vehicle model is a simple rotationally-symmetric body, with a length L of 2.4 m and a width B of 0.2 m. Assuming that the water depth d = 2 m, the free surface is flat without incoming waves. The distance d_1 from the centerline of the submerged vehicle model to the bottom is 0.48 m, and the model

moves at a constant depth and a constant speed V = 1.5 m/s. Due to the relativity of motion, this setting is equivalent to the model remaining stationary while the water flow approaches the body at a velocity of 1.5 m/s. The coordinate system o-xyz is a right-handed coordinate system with the origin located at free surface. The origin o is positioned directly above the center of the model. The x-axis points towards the stern of the body, and the z-axis extends upwards. Computation domain of submerged vehicle in calm water is shown in Fig. 8.

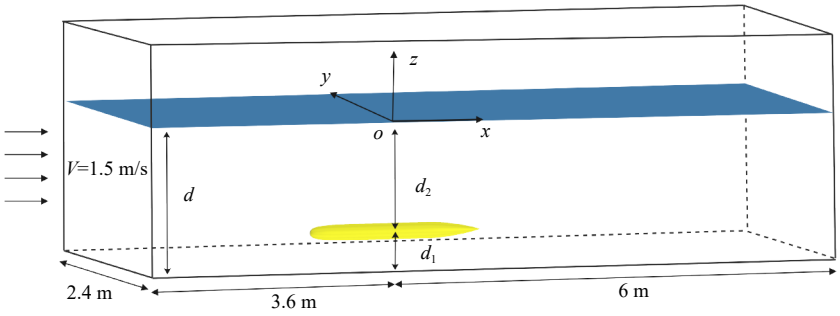

Fig.8 Computation domain of submerged vehicle in calm water

Considering the symmetry of geometry and flow field, only half of the model is modeled in this study to reduce computational cost. The inflow boundary is located at a distance of 2L from the model's centerline, while the outflow boundary at the rear is situated at a distance of 2.5L. The width of the computational domain is set to 1L. The inflow boundary is defined as a velocity inlet, the outflow boundary as a pressure exit, and the top, bottom, and side boundaries are specified as free slip walls. Spatial discretization is performed using trimmed cell mesher and prism layer mesher, with a total of 2.8 million grid nodes. Fig. 9 shows the grids near bow and stern. Prism mesh consists of 5 cell layers. The thickness of the prism layer near the wall is 1.2 mm. As can be seen in Fig. 10, the average y^+ is 45 over the body surface, where the wall function is applicable.

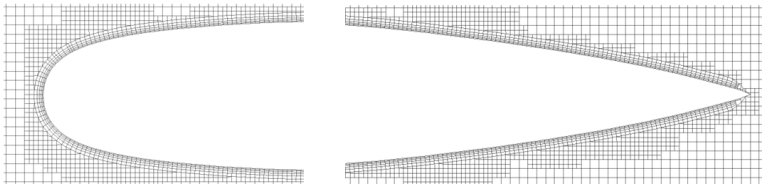

Fig.9 Grids near bow and stern

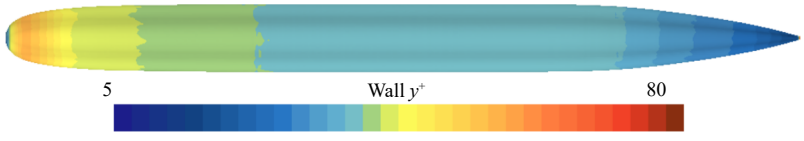

Fig.10 Contour of y+ over the hull

The pressure distribution along the line $z = -d$, $y = 0$ at the bottom is analyzed. Fig. 11 shows comparison of the bottom pressure of the SST turbulence model with the inviscid values and the experimental measured values[14]. The maximum deviation of negative pressure peak is within 9.7%, which is equivalent to the pressure generated by 0.24 mm water column. Due to the Bernoulli effect, the velocity at the front and rear of the model is lower, resulting in higher pressure, whereas the fluid velocity is higher and the pressure is lower in the middle of the model. Consequently, a negative pressure region occurs directly beneath the

vehicle at the bottom. In the figure, the pressure coefficient C_p is defined as:

$$C_p = p/(0.5\rho V^2) \tag{8}$$

where p is the pressure, ρ is the fluid density, and V is the incoming flow velocity.

It can be seen from the figure that the turbulent results, the inviscid results and the experimental measurement values are in good agreement. Both numerical methods can effectively capture the characteristics of the hydrodynamic pressure field of the model. Turbulent simulations considering fluid viscosity and boundary layer development provided more accurate predictions for the stern region than inviscid simulations.

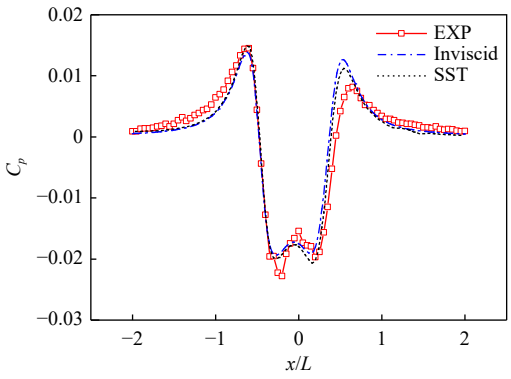

Fig.11 Computed and experimental values of bottom pressure ($z = -d, y = 0$)

Fig. 12 shows the hydrodynamic pressure field of the submerged vehicle at various transverse distances in calm water with SST turbulence model. The hydrodynamic pressure field exhibits a "W"-shaped distribution at line $z = -d, y = 0L$. As the transverse distance increases, the hydrodynamic pressure field takes on a "U"-shaped distribution, with the negative pressure peak diminishing significantly. At $y = 0.75L$, the negative pressure peak is only 1/6 of the value at $y = 0L$. The pressure changes induced by the vehicle's motion are primarily confined within one ship length.

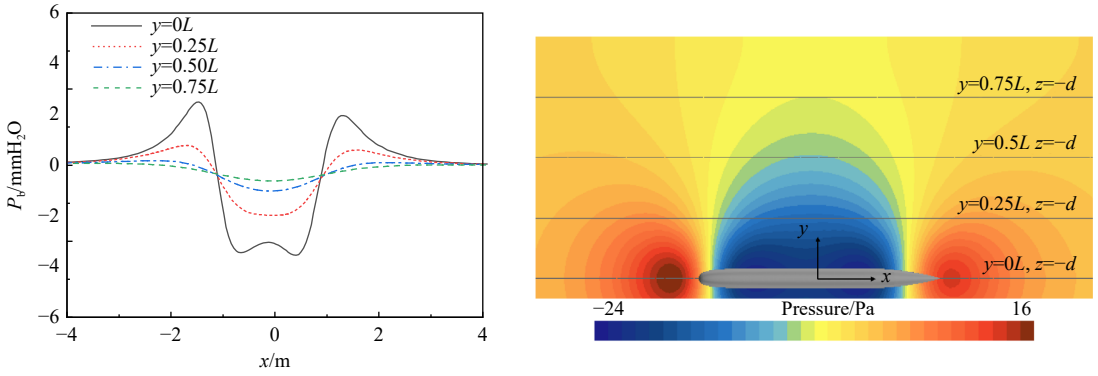

Fig.12 Hydrodynamic pressure field of submerged vehicle at different transverse distances in calm water(z=-d)

2.3 Wave force of a sphere in regular waves

Stokes' fifth-order waves are studied in this section. The wave height H is 0.6 m, the wavelength λ is 6.28 m, the wave period T is 1.92 s. The water depth d is 4 m, the radius R of the sphere is 1 m, and the distance d_1 from the center of the sphere to the bottom is 2 m. The sphere moves to the left at a constant depth and a constant speed V=1.25 m/s.

Fig. 13 shows the computation domain and grids of the sphere in regular waves. Only half of the sphere is modeled in the numerical simulation to reduce computational cost. The spatial discretization is conducted using a trimmed cell mesher, resulting in 3.1 million grid nodes. The inflow boundary is 1.5λ from the sphere, and the outflow boundary is 2.5λ from the sphere. The width of computational domain is 10R to reduce the blocking effect. The size of the domain is shown in the following figure. Both the inflow and outflow boundaries are specified as velocity inlets, the top boundary as a pressure outlet, and the bottom and side boundaries as free slip walls. To ensure the accuracy of the wave simulation, a wave forcing region is established within 1λ of the inflow and outflow boundaries to eliminate wave reflection interference. The

spatial and temporal discretization settings for the computation are the same as those used in the previous study for the regular wave hydrodynamic pressure field computation. Ignoring the viscous effect, the wave force of the sphere is obtained by numerically solving the Euler equation of ideal fluid. The comparison of the numerical solution of the wave force in the x-direction with the analytical solution from Ref.[15] is shown in Fig. 14. The amplitude difference between the wave forces is within 5%.

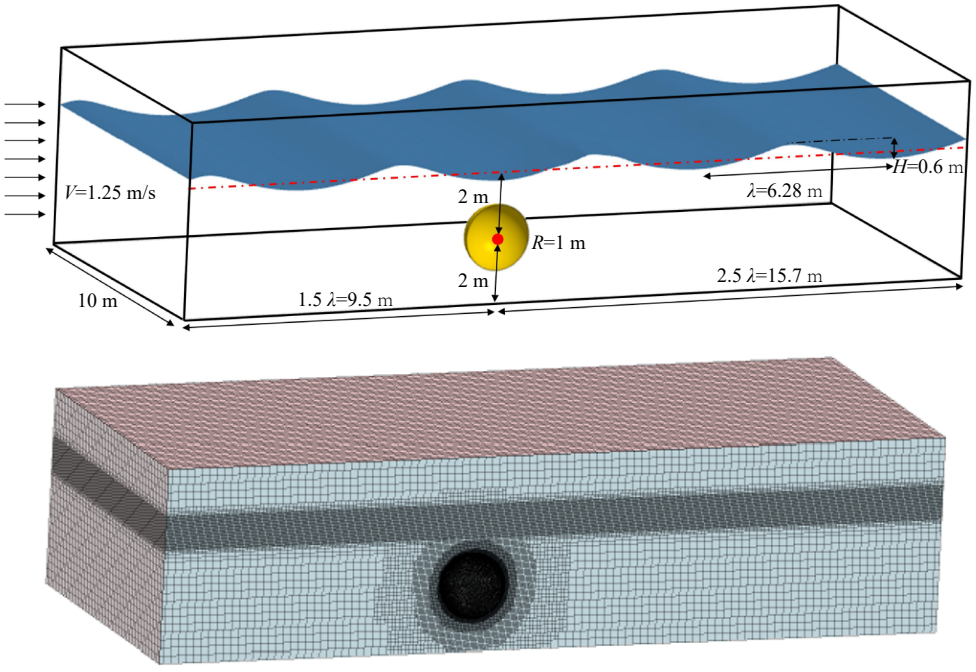

Fig.13 Sphere in regular waves

3 Results and discussion

3.1 Hydrodynamic pressure field of a sphere in regular wave

The hydrodynamic pressure field of regular wave, sphere in calm water and sphere in regular wave are numerically simulated respectively. The wave parameters, sphere geometry and motion parameters are the same as those in the previous simulation of sphere's wave force.

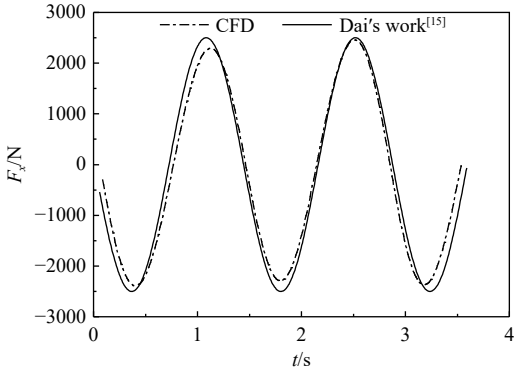

Fig.14 Wave forces on a sphere in regular wave

Fig. 15 shows the pressure distribution at the bottom with different transverse distances when the wave crest passes over the sphere. The black solid lines represent the hydrodynamic pressure field of sphere in regular waves, while the green dashed lines depict the simple linear superposition of wave hydrodynamic pressure field and sphere hydrodynamic pressure in calm water. It is observed that the hydrodynamic pressure field of sphere in waves is not a linear superposition of wave hydrodynamic pressure field and sphere hydrodynamic pressure field in calm water. Beyond a transverse distance of 5 m, the influence of the sphere's hydrodynamic pressure field can be neglected, and the bottom pressure is primarily affected by waves. In the region around $x = -4$ m, the bottom pressure distribution deviates from the wave hydrodynamic pressure field due to the influence of the momentum source term artificially added by the wave forcing.

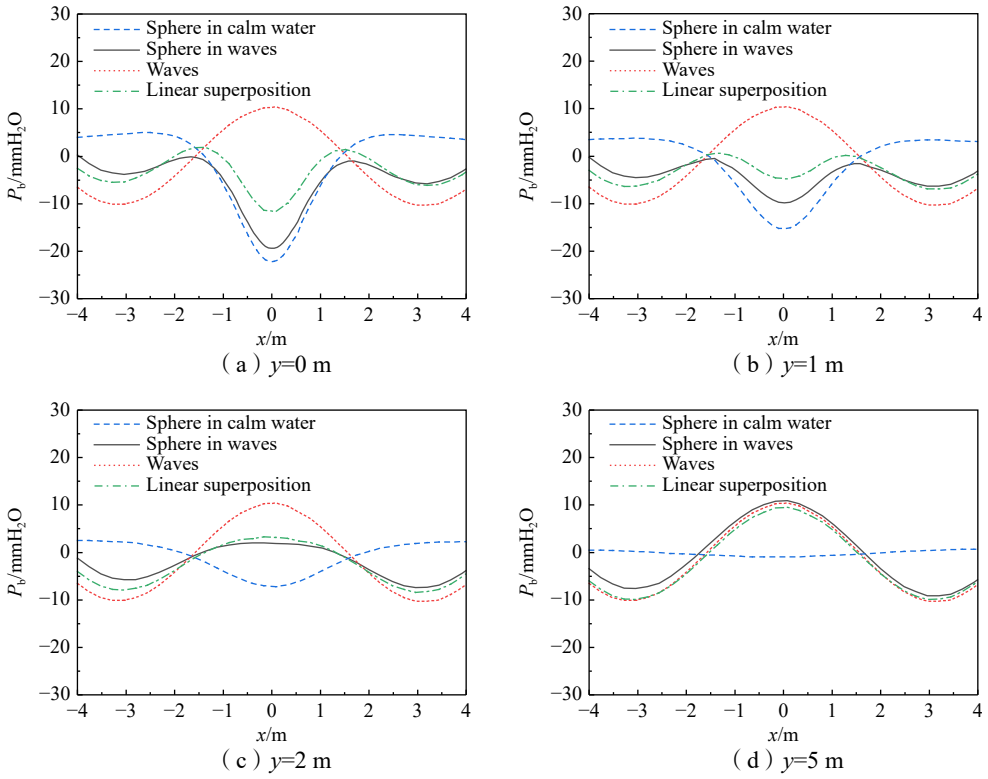

Fig.15 Bottom pressure when the wave crest passes over the sphere ($z = -d$)

Fig. 16 shows the bottom pressure distribution with different transverse distances when the wave trough passes over the sphere. It is observed that the hydrodynamic pressure field of the sphere in waves is not a

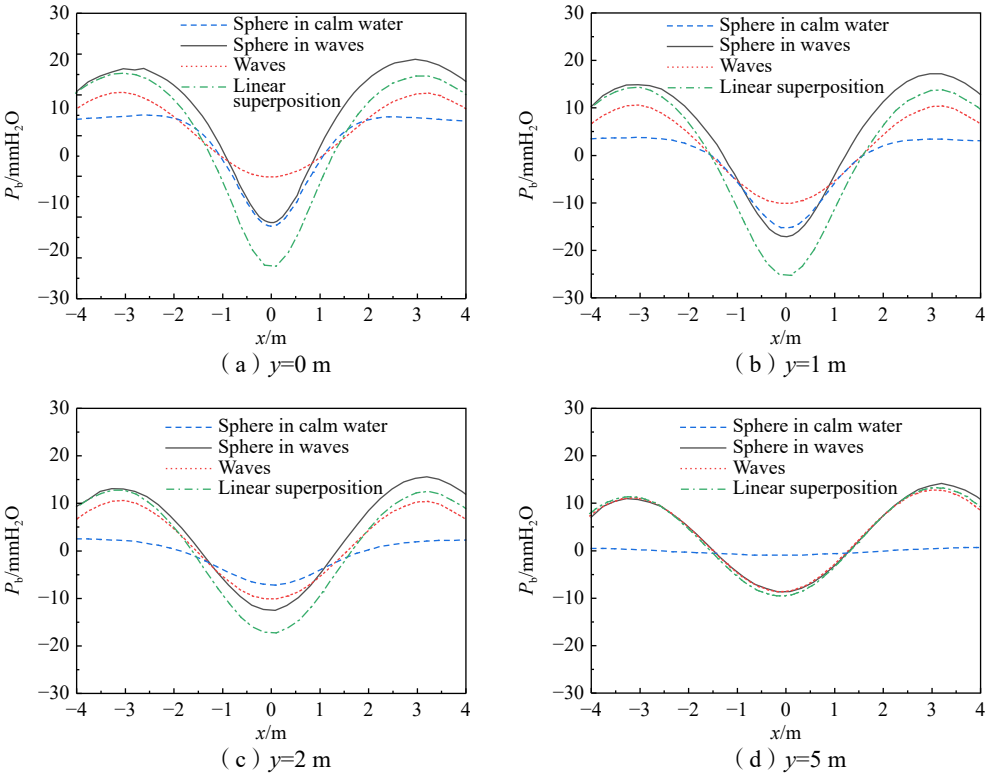

Fig.16 Bottom pressure when the wave trough passes over the sphere ($z = -d$)

linear superposition of wave hydrodynamic pressure field and sphere hydrodynamic pressure field in calm water. At y = 0 m and y = 1 m, the hydrodynamic pressure field of sphere in waves is significantly influenced by sphere, resembling more closely the sphere hydrodynamic pressure field in calm water. At y = 2 m and y = 5 m, the influence of the sphere is weaker, and the hydrodynamic pressure field of sphere in waves is more greatly affected by wave hydrodynamic pressure field.

3.2 Hydrodynamic pressure field of submerged vehicle in regular wave

The hydrodynamic pressure field of submerged vehicle in Stokes' fifth-order wave is numerically simulated. The wavelength is 8.0 m and the wave height is 0.018 m (See Fig. 17). As is shown in Fig. 18, the distance d_1 from the centerline of the submerged vehicle model to the bottom is 0.48 m. The model moves at a constant depth and a constant speed V = 1.5 m/s. Only half of the submerged vehicle model is modeled in the numerical simulation to reduce computational cost. The inflow and outflow boundaries are located at a distance of 1.5λ and 2.5λ from the bow and stern of the submerged vehicle respectively. The spatial discretization is conducted using trimmed cell mesher and prism layer mesher, resulting in 7.7 million grid nodes. Both inflow and outflow boundaries are specified as velocity inlets, the top boundary as a pressure outlet, and the bottom and side boundaries as free slip walls. To ensure the accuracy of the wave simulation, a wave forcing region is established within 1λ of the inflow and outflow boundaries to prevent wave reflection interference.

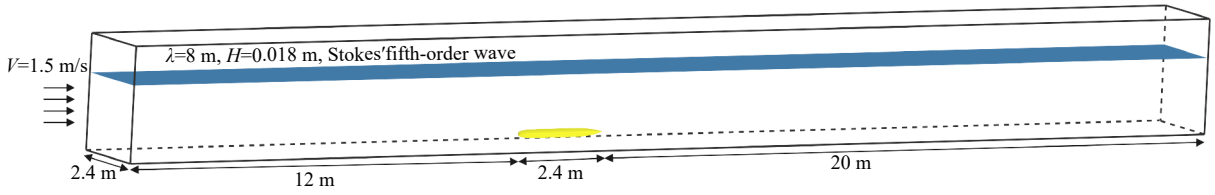

Fig.17 Computation domain of submerged vehicle in regular wave

The SST turbulence model is employed to predict the hydrodynamic pressure field. Assuming the wave crest passes through the origin at t = 0 s, the bottom pressure distribution at various transverse distances is illustrated in Fig. 19. The influence of submerged vehicle's hydrodynamic pressure field is weak at y= 0.5L, and can be ignored at y= 0.75L. The amplitude of the wave hydrodynamic pressure field is significantly greater than that of the submerged vehicle's hydrodynamic pressure field, hence the duration of the maximum negative pressure cannot be used as a criterion for identifying underwater targets. In these instances, alternative approaches, such as signal detection methods based on the frequency domain characteristics of the submerged vehicle hydrodynamic pressure field signals, should be considered.

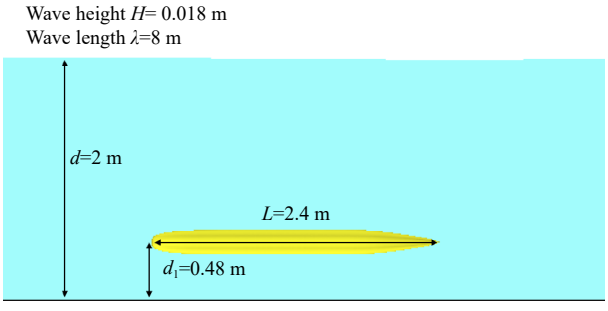

Fig.18 Submerged vehicle in regular waves (d_1=0.48 m)

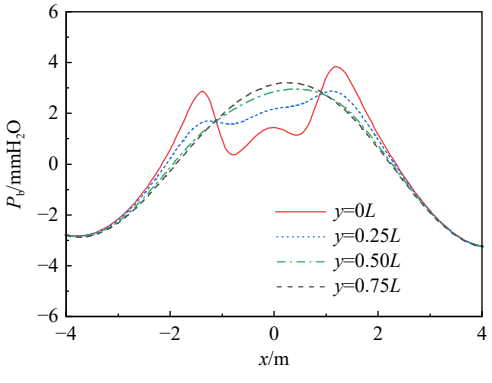

Fig.19 Bottom pressure when t = 0 s (d_1=0.48 m)

Fig. 20(a)–(b) indicate that at $y = 0L$ and $y = 0.25L$, the bottom pressure can be approximated as a simple superposition of wave's bottom pressure field and submerged vehicle's bottom pressure field, with both negative pressure peaks and variation law aligning closely. Fig. 20(c)–(h) shows the variation of hydrodynamic pressure field of submerged vehicle in waves at different time. The hydrodynamic pressure field of

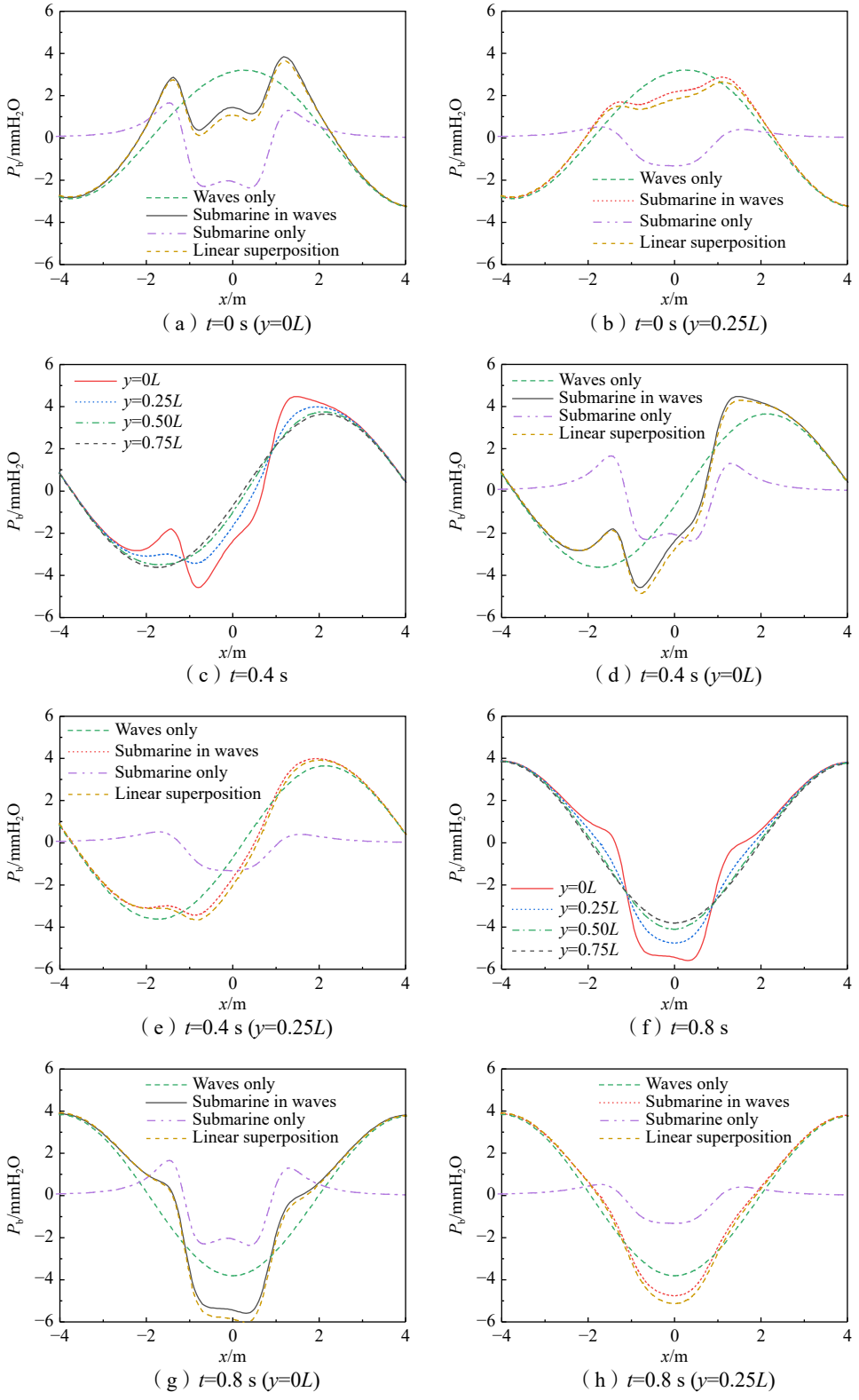

Fig.20 Bottom pressure of submerged vehicle in regular wave varying with time (d_1=0.48 m)

submerged vehicle in waves are approximately consistent with the simple superposition law. Due to the slender nature of the submerged vehicle, the diffraction effect on waves is weak. Simple superposition method can be used to quickly predict the hydrodynamic pressure field of submerged vehicle in waves.

The location of the submerged vehicle is depicted in Fig. 21, where the parameter d_1 has been increased to 0.72 m. Fig. 22 illustrates the variations of bottom pressure at different time. As the distance d_1 increases, submerged vehicle's bottom pressure diminishes. The bottom pressure can be approximated as a simple superposition of wave's bottom pressure field and submerged vehicle's bottom pressure field. Furthermore, the bottom pressure of submerged vehicle in waves is slightly higher than that predicted by the simple superposition method.

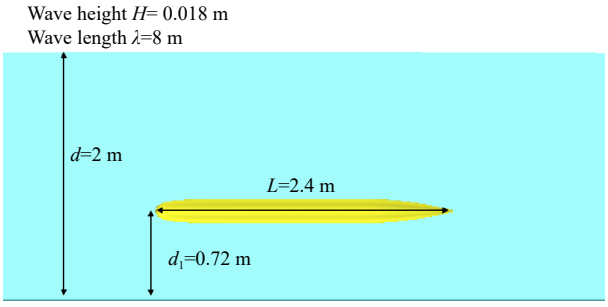

Fig.21 Submerged vehicle in regular waves (d_1=0.72 m)

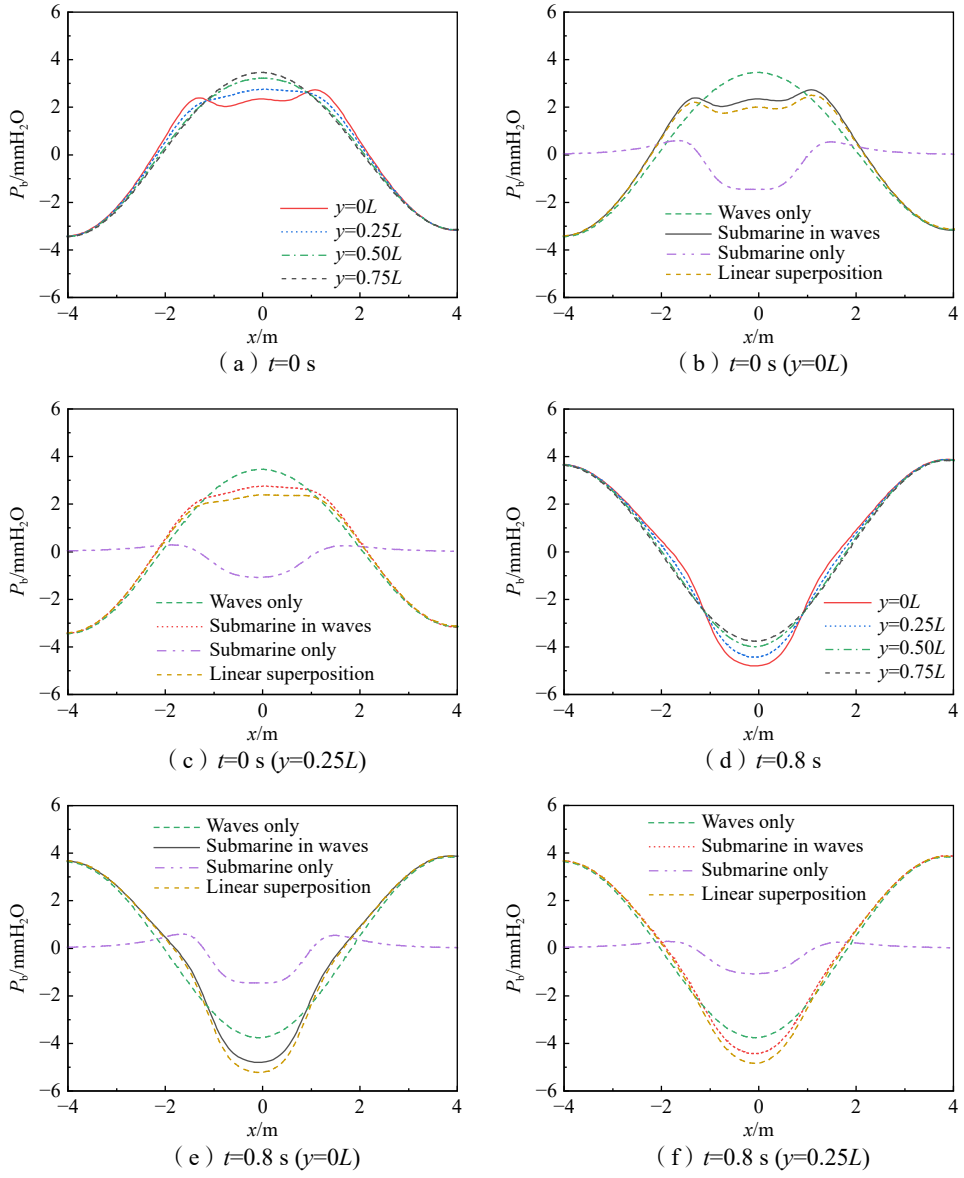

（a）t=0 s （b）t=0 s (y=0L） （c）t=0 s (y=0.25L） （d）t=0.8 s （e）t=0.8 s (y=0L） （f）t=0.8 s (y=0.25L）

Fig.22 Bottom pressure of submerged vehicle in regular wave varying with time (d_1=0.72 m)

The location of the submerged vehicle is depicted in Fig. 23, where the parameter d_1 has been decreased to 0.24 m. Fig. 24 illustrates the variations of bottom pressure at different time. As the distance d_1 decreases, submerged vehicle's bottom pressure increases. The conclusion drawn earlier still holds true. The bottom pressure of submerged vehicle in waves is slightly higher than that predicted by the simple superposition method, with both negative pressure peaks and variation law aligning closely.

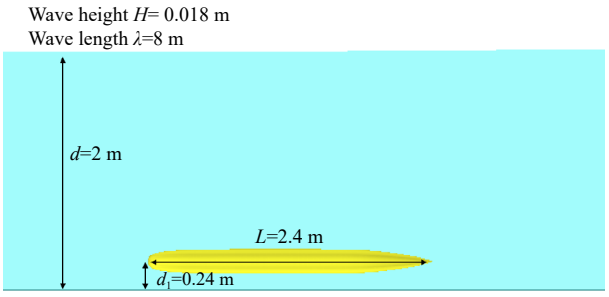

Fig.23 Submerged vehicle in regular waves (d_1=0.24 m)

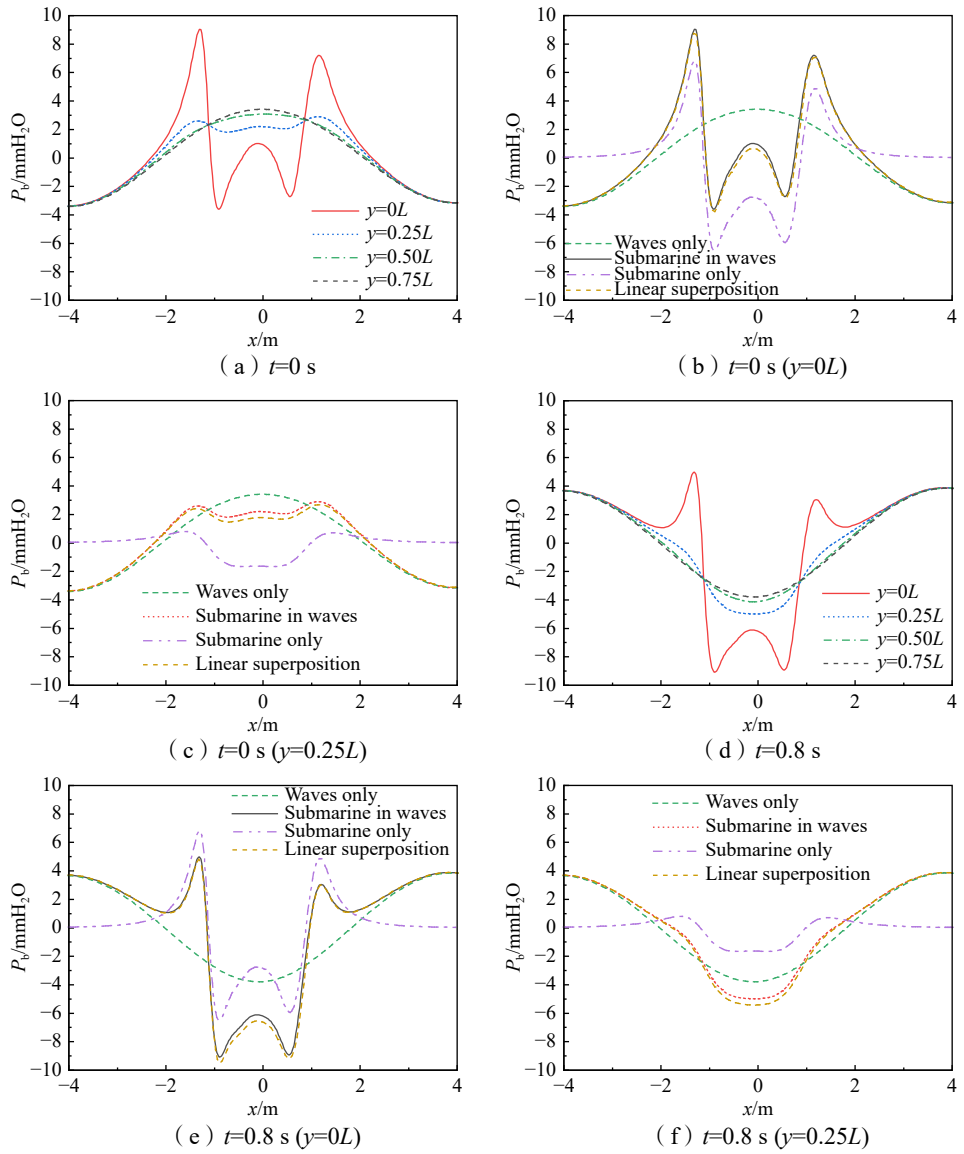

（a）t=0 s　（b）t=0 s (y=0L）

（c）t=0 s (y=0.25L）　（d）t=0.8 s

（e）t=0.8 s (y=0L）　（f）t=0.8 s (y=0.25L）

Fig.24 Bottom pressure of submerged vehicle in regular wave varying with time (d_1=0.24 m)

4 Conclusions

The finite volume method was employed to predict the hydrodynamic pressure fields induced by regular

waves, submerged vehicles in calm water, and submerged vehicles in regular waves. The accuracy of the numerical method was validated through comparisons with tank experimental measurements. The analysis of submerged vehicles' hydrodynamic pressure fields yielded the following conclusions:

Based on the finite volume method, a high-precision wave hydrodynamic pressure field prediction method is established. The deviation between simulation and measured bottom pressure value is below 10% for the regular wave with a wavelength of 8.0 m and a wave height of 0.025 m in a tank with a depth of 2 m. Time discretization employs a second-order implicit scheme with the maximum Courant number throughout the computation maintained below 0.4. The grid spacing in vertical direction is set at 1/16 of the wave height, with a grid aspect ratio below 8. The inflow and outflow boundaries are both set as velocity inlets, with wave forcing applied.

Both inviscid and turbulent computations are capable of predicting hydrodynamic pressure fields of submerged vehicles, with the primary difference being near the stern. Since turbulent computations account for fluid viscosity and the development of boundary layers, the predicted hydrodynamic pressure field values near the stern are closer to measured values. The hydrodynamic pressure field exhibits a "W"-shaped distribution at $z = -d$, $y = 0L$. As the transverse distance increases, the hydrodynamic pressure field assumes a "U"-shaped distribution, with the negative pressure peak diminishing substantially. At $y = 0.75L$, the negative pressure peak is only 1/6 of the value at $y = 0L$. The pressure changes induced by the vehicle's motion are primarily confined within one ship length.

When the magnitudes of the wave hydrodynamic pressure field and the submerged vehicle hydrodynamic pressure field are similar, it can be challenging to identify the submerged vehicle using conventional methods, such as identifying negative pressure peaks or the duration of negative pressure. In these instances, alternative approaches such as signal detection methods based on the frequency domain characteristics of the submerged vehicle hydrodynamic pressure field signals, should be considered.

The diffractive effect of a sphere leads to the hydrodynamic pressure field of a sphere in waves not being a linear superposition of the wave hydrodynamic pressure field and the sphere hydrodynamic pressure field in calm water. The submerged vehicle examined in this study is a slender body with a length-to-width ratio of 12, which displays a relatively weaker diffractive effect on waves. Consequently, the hydrodynamic pressure field of the submerged vehicle in waves is approximately equivalent to the simple superposition of the wave hydrodynamic pressure field and the submerged vehicle hydrodynamic pressure field in calm water. Future research should explore the diffractive effects of submerged vehicles with varying length-to-width ratios.

References

[1] Cheng J, Zhang J, Jiang R, et al. Development status of underwater electromagnetic detection technology[J]. Digital Ocean & Underwater Warfare, 2019, 2(4): 45–49.

[2] Jin Y, Zhang Z, Gu J, et al. Pressure variation on sea bottom caused by vehicle deep in sea[J]. Journal of Wuhan University of Technology (Transportation Science & Engineering), 2013, 37(5): 1098–1101.

[3] Deng H, Zhang Z, Yi W, et al. A mathematical modeling method for an analytical solution of ship hydrodynamic pressure fields in complex restricted waters[J]. Journal of Marine Science and Engineering, 2022, 10(2): 232.

[4] Deng H, Wang K, Zhang Z, et al. A modeling and comparative study of bottom pressure signals generated by waves and ship in shallow water[J]. Ocean Engineering, 2022, 263: 112399.

[5] Jiang R, Zhang X, Shi J. Hydrodynamic pressure field detection technology[M]. Beijing: Weapons Industry Press, 2015. (in

Chinese)
[6] Lyu L, Sun H, Wang J, et al. Ocean wave impact on ship hydrodynamic pressure field based on OpenFOAM[J]. Ship Electronic Engineering, 2014, 34(10): 135–137.
[7] Jiang R, Shi J, Lin C, et al. Real-time detection of ship hydrodynamic pressure field signal based on autoregressive model filtering[J]. Acta Armamentarii, 2009, 30(7): 999–1003.
[8] Versteeg H, Malalasekera W. An introduction to computational fluid dynamics: The finite volume method[M]. New York: Wiley, 1999.
[9] Hirt C W, Nichols B D. Volume of fluid (VOF) method for the dynamics of free boundaries[J]. J. Comput. Phys., 1981, 39(1): 201–225.
[10] Fenton J. A fifth-order Stokes theory for steady waves[J]. Journal of Waterway, Port, Coastal, and Ocean Engineering, 1985, 111(2): 216–234.
[11] Choi J, Yoon S. Numerical simulations using momentum source wave-maker applied to RANS equation model[J]. Coastal Engineering, 2009, 56(10): 1043–1060.
[12] Kim J, O'Sullivan J, Read A. Ringing analysis of a vertical cylinder by Euler overlay method[C]. Proceedings of the ASME 2012 31st International Conference on Ocean, Offshore and Arctic Engineering, Volume 4: Offshore Geotechnics, Rio de Janeiro, Brazil, July 1–6, 2012.
[13] Perić R, Abdel-Maksoud M. Reducing undesired wave reflection at domain boundaries in 3D finite volume–based flow simulations via forcing zones[J]. Journal of Ship Research. 2020, 64: 23–47.
[14] Zhang Z, Gu J, Deng H. Ship hydrodynamic pressure field[M] . Beijing: Science Press, 2016. (in Chinese)
[15] Dai Y, Duan W. Potential flow theory of ship motions in waves[M]. Beijing: National Defense Industry Press, 2008.

规则波中潜航体水底压强场特性研究

易文彬，张志宏，邓　辉，孟庆昌，夏维学，王　冲，李沛豪
（海军工程大学 基础部，武汉 430033）

摘要：为了分析规则波中潜航体水底压强场的变化规律，本文基于有限体积法数值求解规则波水底压强场、静水中潜航体水底压强场及规则波中潜航体水底压强场。通过在数值波浪水槽的边界附近区域添加动量源项迫使 N–S 方程的解趋向于波浪理论解，消除波浪反射等不利影响。基于层流模型、湍流模型和理想流体模型的计算均能较好地捕捉规则波的波形和水底压强分布，与实验测量值吻合较好。在潜航体水底压强场的计算结果中，湍流计算考虑流体黏性和边界层的发展，其在艇尾附近的水底压强预报相比于无黏计算更接近实验测量值。由于圆球的绕射作用，波浪中圆球水底压强场并非波浪水底压强场和圆球水底压强场的线性叠加。细长的潜航体对波浪的绕射作用较弱，波浪中潜航体水底压强场可近似认为是波浪水底压强场和潜航体水底压强场的叠加，进而可以大大简化波浪中潜航体水底压强场的计算和分析。

关键词：规则波；潜航体；水底压强场；数值模拟
中图分类号：U661.1　　**文献标识码：**A
基金项目：海军工程大学自主研发项目（2022501220）；湖北省自然科学基金资助项目（2024AFB954）
作者简介：易文彬（1990–），男，海军工程大学副教授；
邓　辉（1984–），女，海军工程大学教授。